ACS Partner Journal

Journal of the American Society for Mass Spectrometry

pubs.acs.org/jasms

Research Article

Microscopy-Directed Imaging Mass Spectrometry for Rapid High Spatial Resolution Molecular Imaging of Glomeruli

Published as part of the Journal of the American Society for Mass Spectrometry virtual special issue "Focus: High-Throughput in Mass Spectrometry".

Allison B. Esselman, Nathan Heath Patterson, Lukasz G. Migas, Martin Dufresne, Katerina V. Djambazova, Madeline E. Colley, Raf Van de Plas, and Jeffrey M. Spraggins*

Cite This: *J. Am. Soc. Mass Spectrom.* 2023, 34, 1305−1314

Read Online

ACCESS | Metrics & More | Article Recommendations | Supporting Information

ABSTRACT: The glomerulus is a multicellular functional tissue unit (FTU) of the nephron that is responsible for blood filtration. Each glomerulus contains multiple substructures and cell types that are crucial for their function. To understand normal aging and disease in kidneys, methods for high spatial resolution molecular imaging within these FTUs across whole slide images is required. Here we demonstrate a workflow using microscopy-driven selected sampling to enable 5 μm pixel size matrix-assisted laser desorption/ionization imaging mass spectrometry (MALDI IMS) of all glomeruli within whole slide human kidney tissues. Such high spatial resolution imaging entails large numbers of pixels, increasing the data acquisition times. Automating FTU-specific tissue sampling enables high-resolution analysis of critical tissue structures, while concurrently maintaining throughput. Glomeruli were automatically segmented using coregistered autofluorescence microscopy data, and these segmentations were translated into MALDI IMS measurement regions. This allowed high-throughput acquisition of 268 glomeruli from a single whole slide human kidney tissue section. Unsupervised machine learning methods were used to discover molecular profiles of glomerular subregions and differentiate between healthy and diseased glomeruli. Average spectra for each glomerulus were analyzed using Uniform Manifold Approximation and Projection (UMAP) and *k*-means clustering, yielding 7 distinct groups of differentiated healthy and diseased glomeruli. Pixel-wise *k*-means clustering was applied to all glomeruli, showing unique molecular profiles localized to subregions within each glomerulus. Automated microscopy-driven, FTU-targeted acquisition for high spatial resolution molecular imaging maintains high-throughput and enables rapid assessment of whole slide images at cellular resolution and identification of tissue features associated with normal aging and disease.

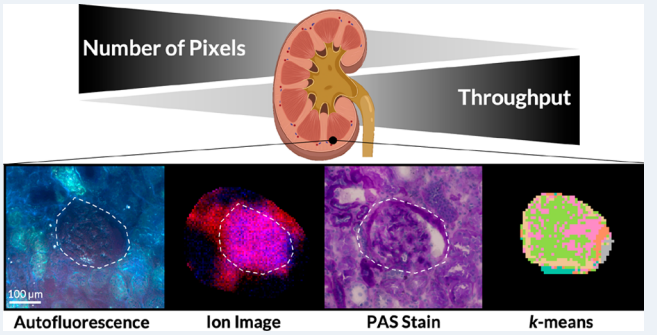

KEYWORDS: *MALDI IMS, multimodal, molecular imaging, high spatial resolution imaging, human kidney, whole slide imaging, high-throughput, glomeruli, targeted, lipids, unsupervised machine learning*

INTRODUCTION

The kidney is a vital organ that filters waste from the blood, regulates the flow of electrolytes, maintains bodily pH, reabsorbs nutrients, removes waste, and produces urine.[1,2] These processes take place in roughly one million nephrons that span the cortex and medulla. The filtration process occurs at the start of the nephron, the glomerulus, which is a spherical, multicellular functional tissue unit (FTU) with a diameter of ∼200 μm.[2,3] A glomerulus contains important substructures such as fenestrated endothelium, glomerular basement membrane, and podocytes, among others. Modifications in the glomeruli's ability to perform filtration is at the center of various kidney diseases such as Alport syndrome and diabetic nephropathy.[4−6] The former can cause glomerular damage, which leads to alterations in glomerular substructures, such as the basement membrane. Grove et al. demonstrated an increase in lysophospholipid and ganglioside species in glomeruli of mice with diabetic nephropathy.[5] The ability to link molecular drivers to specific cell types and structures in the glomerulus is necessary for fully understanding kidney disease, yet this remains a challenge due to the spatial scales and complexity of the affected cellular neighborhoods.[7,8]

Received: January 30, 2023
Revised: May 30, 2023
Accepted: June 1, 2023
Published: June 15, 2023

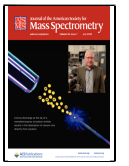

Liquid chromatography mass spectrometry (LC-MS) is the traditional approach for identifying and quantifying proteins, peptides, lipids, and metabolites from whole tissue sections.[9] Laser capture microdissection (LCM) can be combined with LC-MS to gain molecular information for specific functional tissue units, such as glomeruli; however, no spatial information is learned about the molecular distribution within these functional tissue units or their surrounding neighborhood.[10] Imaging mass spectrometry (IMS) can offer relative quantitative information while also providing high spatial resolution, *in situ* maps of hundreds to thousands of molecular species.[11,12] IMS measurements can be coregistered with microscopy, providing morphological as well as cellular context to IMS molecular images. This multimodal approach enables comprehensive molecular histology of normal and diseased tissues.[13]

Matrix-assisted laser desorption/ionization (MALDI) is one of the most common IMS technologies for high spatial resolution molecular imaging.[7] Briefly, MALDI IMS is performed by mounting a thin tissue section onto a glass slide and coating the sample with a UV-absorbing small molecule (matrix). The sample is desorbed and ionized by laser irradiation at specific positions across the sample surface, referred to as pixels. A mass spectrum is acquired at every position, and heatmap-like images can be generated for each detected molecule, reporting its intensity across the sampled tissue area. The ability to deliver untargeted, highly multiplexed molecular information while maintaining high spatial integrity in tissues makes IMS ideally suited for discovering relationships between molecular distributions and cellular organization, structure, and signaling.[14] Although significant efforts have been made to improve sample preparation and storage,[15] molecular coverage,[16] specificity,[17] and spatial resolution[17−19] for kidney analysis, further work is needed to routinely investigate molecular changes on a cellular level in complex tissue structures, like the nephron.[20]

A crucial component of investigating small biological features is spatial resolution.[20−22] In MALDI IMS, spatial resolution is determined by the diameter of the laser at the sample surface, the pitch or movement of the stage from one pixel to another, and the degree of molecular delocalization that occurs during sample preparation.[18,23,24] Modern MALDI imaging platforms can routinely achieve 10 μm pixel sizes with "front-side" laser optics[17,18,20] and <1 μm using custom "transmission geometry" ion sources.[25−27] Continued improvement in spatial resolution is necessary to fully investigate the molecular profiles of cell types and FTUs with MALDI IMS, which is especially important for uncovering the molecular drivers of glomerular diseases.

Imaging whole tissue sections at high spatial resolution entails large numbers of pixels and requires significant data acquisition times, increasing the cost and instrument wear for IMS experiments.[28] Multimodal approaches using complementary microscopy to strategically target structures can greatly reduce the number of pixels imaged and improve throughput. Previously, Patterson et al. demonstrated a histology-directed approach to annotate glomeruli in human kidney sections using label-free autofluorescence microscopy.[29,30] The ability to define measurement regions with unstained imaging approaches, such as autofluorescence microscopy, can be used to guide IMS experiments for a variety of tissue types.

Here we advance this work by using human kidney tissue as a case study to enable automated tissue feature detection and the creation of IMS measurement regions for high spatial resolution molecular imaging. Specifically, we use a deep learning model to detect and segment glomeruli across whole slide autofluorescence kidney tissue images. These segments are then translated into glomeruli-specific IMS measurement regions, avoiding the need to obtain IMS data from nonglomerular tissue. This allows for virtually all glomeruli (100s) to be imaged at 5 μm spatial resolution without acquiring data from the entire tissue section. This approach incorporates previously established imaging techniques and new intelligent data acquisition strategies to enable rapid, high spatial resolution MALDI imaging of targeted functional tissue units.

EXPERIMENTAL SECTION

Materials. Ammonium formate and a periodic acid-Schiff (PAS) stain kit were bought from Sigma-Aldrich (St. Louis, MO). 4-(dimethylamino)cinnamic acid (DMACA) with 99% purity was bought from Thermo Scientific (Waltham, MA). High-performance liquid chromatography (HPLC)-grade acetone was purchased from Fisher Scientific (Pittsburgh, PA). Human kidney samples are from the Cooperative Human Tissue Network at Vanderbilt University Medical Center.

Human Kidney Sample Preparation. A normal portion of a kidney cancer nephrectomy from a 53-year-old white male with a BMI of 23 was studied. The pathology assessment of this sample can be found in Table S1. Human kidney blocks were embedded in carboxymethylcellulose (CMC), flash frozen in a bath of isopentane and dry ice, and stored in a −80 °C freezer.[31] Tissue was cryosectioned at a 10 μm thickness using a CM3050 S cryostat (Leica Biosystems, Wetzlar, Germany). The section was thaw-mounted onto indium tin oxide (ITO) coated glass slides (Delta Technologies, Loveland, CO). Autofluorescence images were taken of the section prior to IMS sample preparation with standard DAPI, eGFP, and DSRed fluorescent filters using a Zeiss AxioScan.Z1 slide scanner (Carl Zeiss Microscopy GmbH, Oberkochen, Germany), equipped with a Colibri7 LED light source. To remove endogenous salts, the section was then washed with chilled (4 °C) 150 mM ammonium formate 3 times for 45 s each and then dried with nitrogen gas to remove excess solution. An in-house developed sublimation device was used to sublimate 5 mg of 4-(dimethylamino)cinnamic acid (DMACA) onto the slide while heating (190 °C) for 10 min at a vacuum of 110−150 mTorr and cooling the sample to −78 °C using a dry ice and acetone slurry in the coldfinger, for a final density of ∼0.22 μg/mm^2.[32] The vacuum was broken once the sample returned to room temperature. After MALDI IMS data acquisition, a post-IMS autofluorescence image was acquired on the tissue section prior to matrix removal using a Zeiss AxioScan.Z1 fluorescence slide scanner that uses the previously described eGFP fluorescence filter and a monochromatic brightfield image.[33] After collection of the post-IMS autofluorescence image, the sections were stained with a PAS stain using a standard protocol.[34]

Glomerular Segmentation. Segmentation of glomeruli was performed using previously described methods.[30] Briefly, several glomeruli in the pre-IMS autofluorescence images were manually annotated using polygon regions in QuPath[35] (a whole slide image visualization platform), and these masks and tiles were exported for the training (and testing) of a deep

https://doi.org/10.1021/jasms.3c00033
J. Am. Soc. Mass Spectrom. 2023, 34, 1305−1314

learning model that recognizes glomeruli based on an autofluorescence image input.[35] Specifically, a Mask-RCNN (101 ResNet backbone) convolutional neural network, as implemented in the detectron2 package,[29,30] was trained to deliver glomeruli segmentations based on an autofluorescence image. Evaluation of the model's performance was conducted where manual annotations were compared against automated annotations delivered by the convolutional neural network and their overlap was computed using the Dice-Sorensen coefficient. High coefficient performance indicated that automated segmentation by a neural network successfully matched and replicated manual annotation. In translating the automatically generated glomeruli segments into data acquisition regions for IMS, the segmented glomeruli areas were scaled by a factor of 1.4 using an affine scale transform to allow for errors in spatial targeting and to ensure capture of the border of each glomerulus. Because of this, some measurement regions contained more than one glomerulus. The automatically generated glomeruli segmentations were manually reviewed in QuPath, and the coordinate file of the segmentations was saved as a .geojson. Measurement regions are defined at the instrument using an optical image ("teach image") that is aligned to the sample carrier positions, a process often referred to as "Teaching the Sample". Here, the autofluorescence tissue image used for glomerular segmentation was also used to teach in FlexImaging. The teaching image is slightly altered during this process by FlexImaging; therefore, a Python script using *wsireg*[36] registered a copy of the original autofluorescence tissue image with the image after teaching. The Python script then transformed the segmentation coordinates (stored in geojson) to the FlexImaging teach image. Once transformed, a modified FlexImaging .mis file containing the instrument method, stage raster size (i.e., pixel size), project name, and glomerular ROIs was created automatically. Practically, the script takes the transformed coordinate positions of the glomeruli segmentation on the modified teach image and translates them into the XML format FlexImaging uses, giving each an enumerated, unique measurement region name.

MALDI IMS. This experiment was performed on a prototypical timsTOF fleX mass spectrometer (Bruker Daltonik, Bremen, Germany). Tissue imaging data from 747,214 pixels and 229 regions were collected at 5 μm IMS pixel size using 60 shots per pixel and 9% total laser power averaging ~27 pixels/second. Data were collected in negative ionization qTOF mode from m/z 450 to 2000. Instrument specific parameters are listed in Table S2. Molecular identification was done using LC-MS/MS and on-tissue MS/MS (see Methods S1, Table S3, and Figures S1−S10). Selected IMS peaks were then annotated using mass accuracy (<5 ppm) to link LC-MS/MS data to ion images (see Table S4 for details).

Rat Brain Homogenate Sample Preparation. Rat brain homogenate was used as a tissue standard for comparison of 5 μm versus 10 μm pitch (i.e., pixel size). Tissue homogenates were cryosectioned at 10 μm thickness and thaw-mounted onto ITO-coated glass slides. The sections were washed with ammonium formate and sublimated with the same protocol as for the human kidney sample. MALDI IMS experiments were performed in triplicate at a 5 and 10 μm stage raster with the same instrument parameters as was done with human kidney. Imaging data were opened in DataAnalysis, and an average mass spectrum for each data set was generated. The DataAnalysis generated peak list from each data set was uploaded to LipidMaps database.[37] The identifications list from the LipidMaps database was narrowed down by only accepting identifications with an absolute ppm error <5 and removing duplicates. The average, standard deviation, and p-value from a two-tailed paired t test of the average total ion current, m/z 885.55 intensity, and lipid identifications were calculated in Excel. The laser ablation craters on the MALDI matrix layer were captured with brightfield microscopy using a Nikon Eclipse 90i microscope (Nikon Instruments Inc., Melville, NY) at 40× magnification. The diameter of each crater was measured using Nikon's NIS-Elements AR 4.11.00 software.

Multimodal Image Registration and Data Analysis. MALDI IMS and microscopy images were recorded in a two-step process. First, laser ablation marks, as measured by the post-IMS autofluorescence image, were aligned to MALDI IMS pixels using *IMS MicroLink*[38] by manually selecting corresponding pairs of laser ablation marks and IMS pixels. Additional microscopy images were then registered to the IMS data via the previously registered post-IMS autofluorescence images in the *wsireg* software.[36] All registered whole slide images were stored in the vendor neutral pyramidal OME-TIFF format and maintain their original spatial resolution (i.e., there is no downsampling or loss of pixel spacing through the registration process).[39] After alignment of all images, automated glomeruli segmentations, as delivered by the neural network, were used to find the MALDI IMS pixels associated with each detected glomerulus and were extracted for further data analysis.

MALDI-IMS Data Preprocessing. Data were exported from Bruker timsTOF file format (.d) to a custom binary format for ease of access and improved performance. Each pixel/frame contains between 10^4−10^5 centroid peaks that cover the entire acquisition range and can be reconstructed to form a pseudoprofile mass spectrum using Bruker's SDK (v2.21).[40] The data set was m/z aligned using internally identified peaks (6 peaks that appeared in at least 50% of the pixels) using the *msalign* library (v0.2.0).[41] This step corrects spectral misalignment (drift along the m/z domain), resulting in increased overlap between spectral features (peaks) across the experiment. Subsequently, the mass axis of the data set was corrected, using theoretical masses for the 6 peaks, to approximately ±1 ppm precision. After alignment and calibration, an average mass spectrum based on all pixels belonging to the glomeruli in the data set was computed. The spectrum was peak-picked, and 714 peaks were detected and used for further analysis. Isotopes were not removed and were allowed to take part in the dimensionality reduction workflow. Following the preprocessing steps, we computed normalization correction factors using a total ion current (TIC) approach. The resulting average spectrum had a mass resolution of ~40,000 at m/z 885.55.

Unsupervised Analysis. Uniform Manifold Approximation and Projection (UMAP) and k-means clustering was used to determine molecular trends among the measured glomeruli.[42] UMAP aims to preserve the global neighborhood structure of the data while reducing it from the original 714-dimensional space to a lower number of dimensions to enable easier visualization that captures broader trends in the data. Clustering groups tissue features or pixels together based on the similarity of their molecular profiles.

https://doi.org/10.1021/jasms.3c00033
J. Am. Soc. Mass Spectrom. 2023, 34, 1305−1314

Analysis was performed at the FTU-level by treating each detected glomerulus (268 in total) as an observation and using the list of 714 peaks as features. The average mass spectrum for each glomerulus was extracted, and all 714 features were integrated with a ± 3−5 ppm window. In addition, pixel-wise clustering was performed, where each pixel was treated as an observation. A total of 714 features were extracted for the mass spectrum of each pixel with a ± 3−5 ppm window. Pixels outside of the glomeruli were excluded from the analysis.

UMAP[43] projection was performed in Python using the *umap-learn* library (v0.5.2) and *k*-means clustering using *scikit-learn* (v1.2.0).[44] UMAP has a large number of hyperparameters; however, only several have a substantial impact on the final embedding. The low-dimensional embedding shown in this paper was obtained by using 3 target dimensions (*n_component* = 3), the *cosine* distance metric (*metric* = 'cosine'), 5 neighbors (*n_neighbors* = 5), and a minimal distance of 0.1 (*min_dist* = 0.1). The low-dimensional representation of the data was subsequently clustered using the *k*-means clustering algorithm with 7 clusters (*n_clusters* = 7). These parameters were obtained by performing a grid search of approximately 150 parameter configurations where *n_neighbors*, *min_dist*, and *n_clusters* were permuted from a subset of available options. The final configuration was selected by empirical examination of the embedding and spatial distribution of the clusters. Pixel-wise clustering was optimized similarly. The entire data set (excluding pixels outside of the glomeruli) was clustered using *k*-means clustering algorithm with 6 clusters (*n_clusters* = 6).

RESULTS AND DISCUSSION

5 μm MALDI Imaging Mass Spectrometry. High spatial resolution MALDI IMS (<10 μm pixel size) increases our ability to study molecular distributions of specific cell types within tissues. Achieving high spatial resolution with current commercial IMS platforms is difficult due to limitations in focusing the MALDI laser at the sample surface and inconsistencies in stage movements. This often leads to oversampling, where adjacent laser ablation craters overlap one another. This can cause signals from one pixel to carry over into another and diminish signal intensity, reducing image quality and molecular coverage.[45] To align the laser in our system, the ion intensity versus focus position of the lens inside the laser was measured. The maxima of the intensity peak should be centered between 85 and 88% focus position. If not, the stage offset value as well as the ring lens above the source were adjusted until the maxima were at the correct focus position. As demonstrated in Figure 1A, the laser ablation crater had a diameter of ∼4.7 μm. To verify that this was sufficient to perform imaging at 5 μm spatial resolution with minimal oversampling, a series of experiments were performed to compare signal intensity using a 5 and 10 μm pitch. Triplicate experiments using a 5 and 10 μm pitch were performed on rat brain homogenate. The 5 μm experiments included ∼2,000 pixels from an area of ∼0.04 mm^2, and the 10 μm experiments covered roughly the same area with ∼500 pixels each. For each experiment, the total number of lipid identifications with a mass error <5 ppm using the LipidMaps database[37] (Figure 1B), average total ion current (Figure 1C), and base peak intensity (Figure 1D) were evaluated. The averages of each triplicate experiment were compared with a 2 tailed paired *t* test to determine if there was a significant difference between the 5 and 10 μm experiments (Table S5).

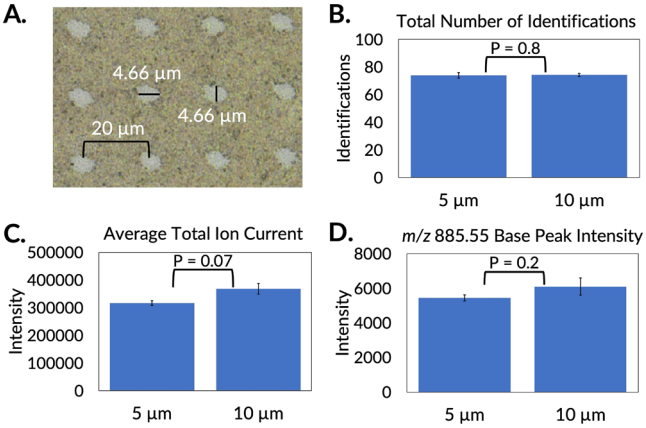

Figure 1. Assessment of oversampling for 5 μm MALDI mass spectrometry. (A) Laser ablation of a matrix-coated slide using a 20 μm pitch shows the ablation craters to be <5 μm in diameter when using 9% total laser power and 60 laser shots. (B) The comparison for total number of identifications, (C) average total ion current, and (D) intensity of the base peak show *p*-values from the *t* test being >0.05, which suggests that there is no significant difference between the 5 and 10 μm experiments. All experiments were performed in triplicate.

The *p*-value from the *t* test was above 0.05 for all three categories, suggesting that there was no significant difference in the average total ion current, base peak intensity, or number of identifications between the 5 and 10 μm pitch experiment. These results indicate that minimal oversampling occurred using our 5 μm pixel MALDI IMS workflow.

High-Throughput, Microscopy-Driven Sampling. Using the trained deep learning segmentation model, 268 glomeruli were automatically segmented in the autofluorescence image from a whole slide human kidney tissue section (Figure 2A). Automating the segmentation process eliminates human drift, reduces human bias, keeps annotations consistent throughout the tissue section, and allows for comprehensive FTU segmentation across expansive tissue areas and large numbers of tissue samples. Additionally, the overall throughput of the workflow is substantially improved by the glomeruli being automatically detected rather than requiring manual annotation of each glomerulus.

The automated glomerular annotations were translated into measurement regions for high spatial resolution MALDI IMS data acquisition (Figure 2B). To account for any inaccuracy in sample registration, each measurement region was computationally scaled to include an expanded border around the glomerular segmentation to ensure the IMS experiment captured the entire FTU. A total of 747,214 (5 μm × 5 μm) IMS pixels were collected from the 268 glomeruli, requiring 7 h and 40 min of data acquisition. Note, this is a significant improvement in throughput relative to traditional imaging methods, where nonglomerular tissue would also be measured. To image the entire kidney tissue section used in this experiment at 5 μm spatial resolution would require 6,645,708 pixels and almost 3 days of acquisition time for the whole tissue section on the same imaging platform (∼30 pixels/second). This demonstrates just how much time can be saved using multimodal, selected sampling approaches, enabling larger tissue areas and, in turn, greater numbers of targeted FTUs to be analyzed. Furthermore, because the total number of pixels is greatly reduced, the resulting file sizes are also

https://doi.org/10.1021/jasms.3c00033
J. Am. Soc. Mass Spectrom. 2023, 34, 1305−1314

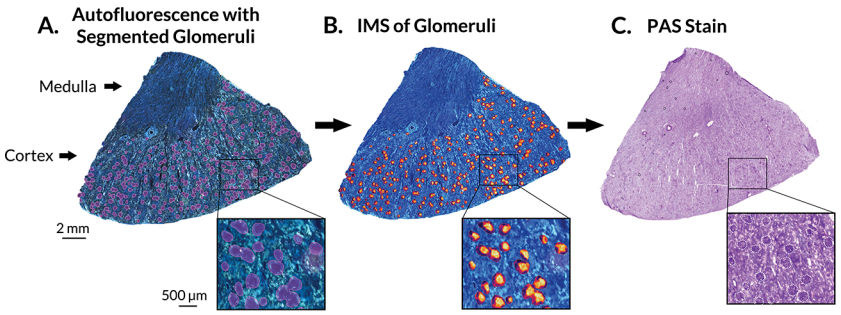

Figure 2. High-throughput workflow for 5 μm MALDI IMS of glomeruli in human kidney tissue. (A) Segmented glomeruli using autofluorescence microscopy are shown with the purple annotations. (B) MALDI IMS was performed on each segmented glomerulus across the whole slide image. (C) After MALDI IMS, the matrix was removed and the tissue was stained with PAS.

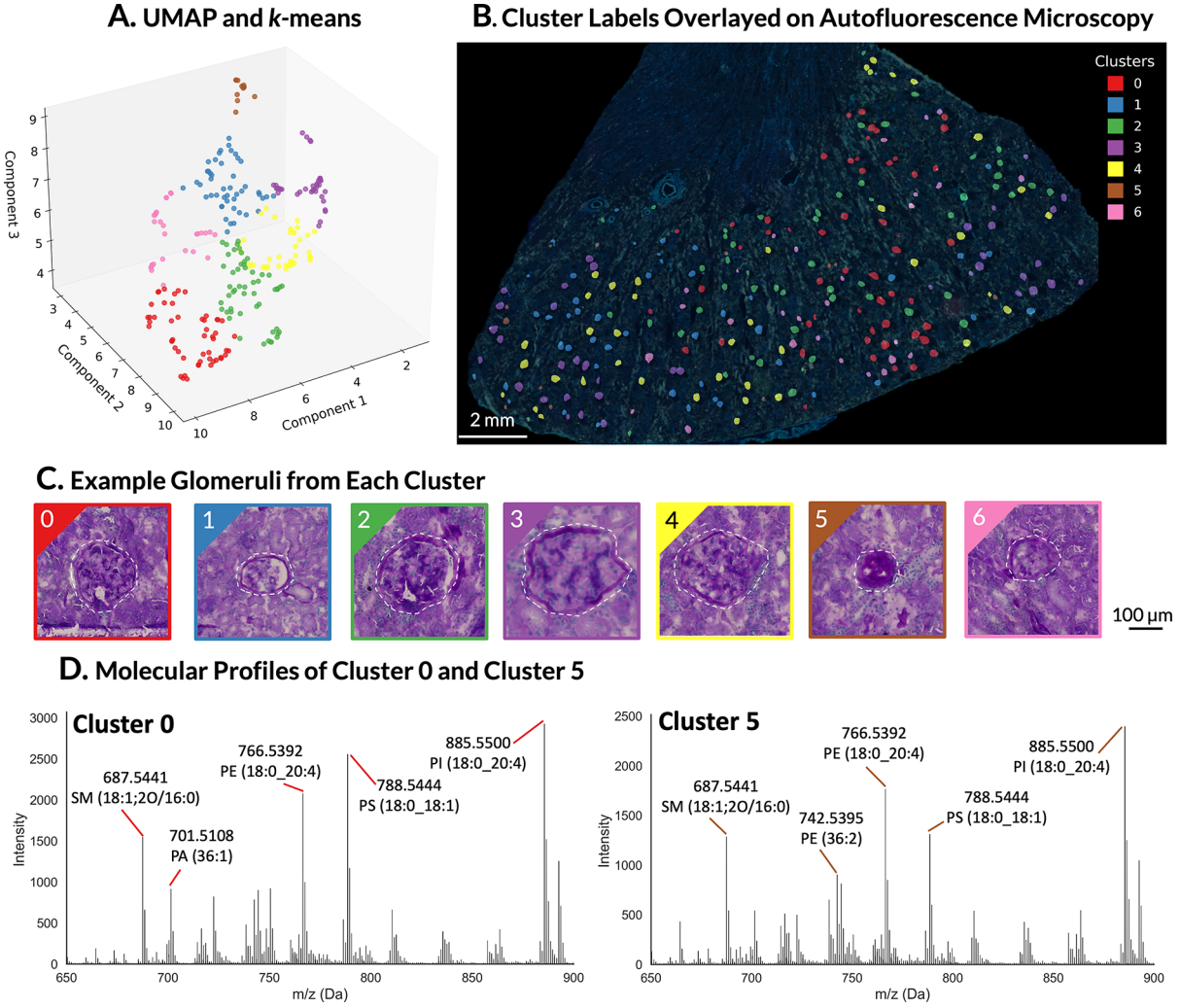

Figure 3. Assessment of healthy and diseased glomeruli using UMAP dimensionality reduction followed by *k*-means clustering. (A) Three-dimensional UMAP plot showing the separation between each of the 7 clusters determined by *k*-means. (B) Each cluster is color-coded, and data are overlaid onto the autofluorescence microscopy image showing the distribution of each cluster in tissue. The scale bar is equal to 2 mm. (C) PAS-stained microscopy images of selected glomeruli from each cluster showing their morphological differences. All PAS images are scaled similarly. The scale bar is equal to 100 μm. (D) Molecular profiles of two clusters of glomeruli showcasing the differences in the relative abundance of selected ions between normal (cluster 0) and diseased (cluster 5) glomeruli.

significantly smaller, requiring less computational resources and time for subsequent analysis.

Because all measurement regions are linked directly to microscopy data, any other imaging modalities that can be coregistered with the autofluorescence image can be integrated and used to guide analysis and interpretation. Following MALDI IMS, the matrix was removed, and the tissue was stained with PAS, commonly used by pathologists as a kidney

https://doi.org/10.1021/jasms.3c00033
J. Am. Soc. Mass Spectrom. 2023, 34, 1305−1314

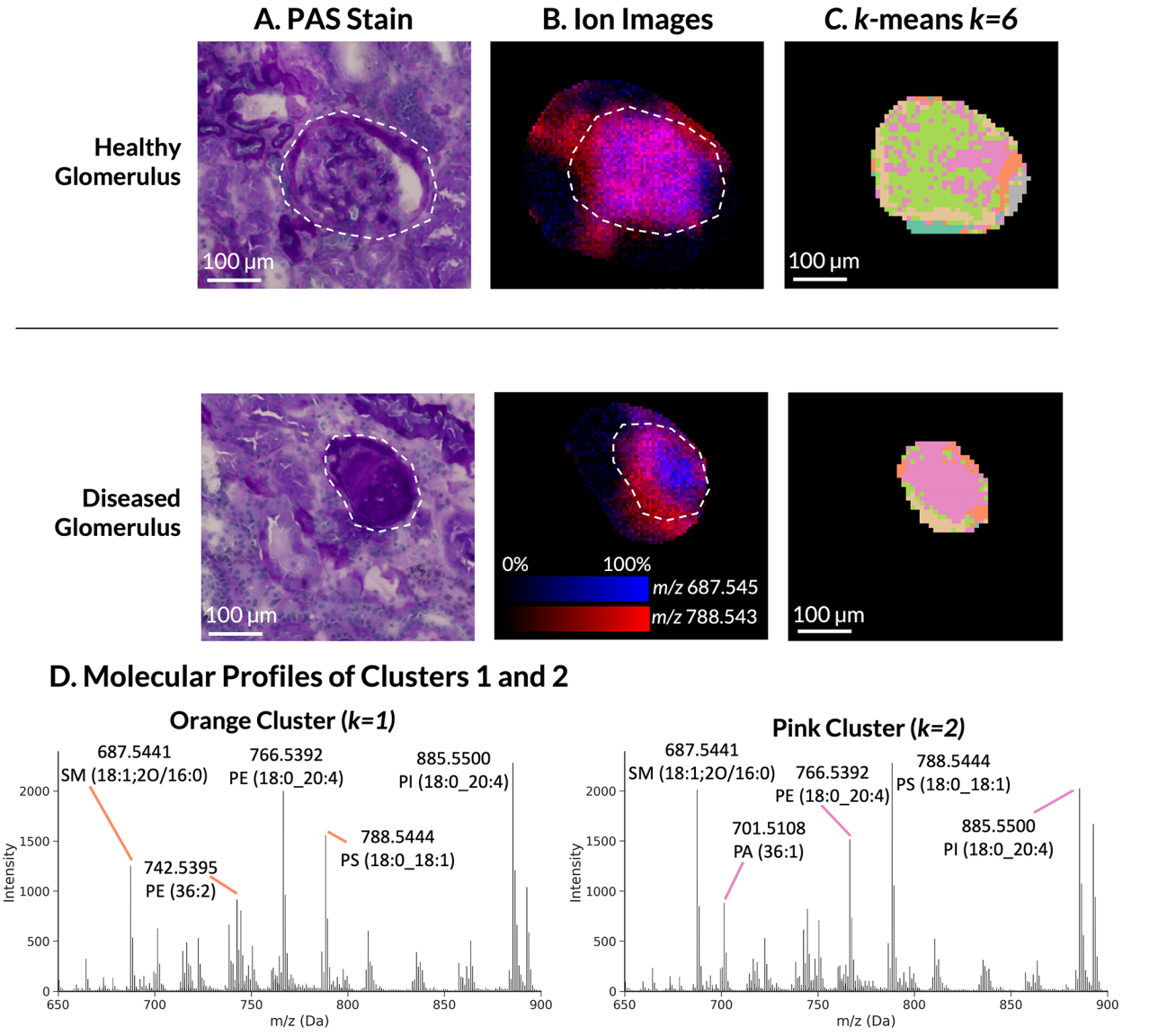

Figure 4. High spatial resolution MALDI IMS data from healthy and diseased glomeruli. (A) PAS stained images showing differences in morphology for each glomerulus—healthy (top) and diseased (bottom). (B) 5 μm MALDI IMS enables visualization of heterogeneous molecular distributions within individual FTUs. Overlaid ion images of SM (18:1;2O/16:0) (m/z 687.5441, 0.3 ppm) and PS (18:0_18:1) (m/z 788.5444, 1.0 ppm) are shown. (C) Multivariate analysis using k-means clustering (k = 6) and reveals molecular subregions in each glomerulus. (D) Molecular profiles of prominent k-means clusters 1 (orange) and 2 (pink). The diseased glomerulus has a higher proportion of pixels that fall into cluster 2 whereas the healthy glomerulus has proportions of pixels associated with clusters 1 (orange), 2 (pink), and 3 (green). Selected peaks from each profile are annotated to highlight differences in the relative abundance between the clusters. All images are scaled similarly. The scale bars provided are equal to 100 μm.

morphology stain (Figure 2C). The ability to acquire MALDI imaging data at 5 μm pixel size and to coregister these data with complementary microscopy allow more exact connections to be made between *in situ* molecular observations and cellular content.

Differentiation of Healthy and Diseased Glomeruli. To first provide a global assessment of the data, an average mass spectrum was calculated per glomerulus, and the glomeruli-specific spectra were partitioned into clusters using unsupervised machine learning. Specifically, dimensionality reduction was performed using UMAP, taking the data set from a 714-dimensioinal space to a 3-dimensional space, followed by k-means clustering in the latter space (Figure 3A). From this analysis, the 268 glomeruli were organized into 7 distinct clusters, which were color-coded and overlaid onto the multimodal imaging data to visualize their spatial distribution within the tissue (Figure 3B). Co-registering the clustering results with the imaging data allowed for a qualitative assessment of the members of each cluster. By comparing the clusters to the associated PAS stain, many of the clusters differentiated healthy and diseased glomeruli (Figure 3C). For example, glomeruli found in cluster 0 were considered healthy with a normal morphology, whereas those found in cluster 5 were all globally sclerosed. The molecular profiles for all the glomeruli in clusters 0 and 5 are shown in Figure 3D with the prominent peaks annotated to highlight differences in their relative abundance. Molecular profiles for all UMAP/k-means clusters can be found in Figure S11.

We hypothesize that the clustering results capture a combination of the disease severity and differences in the

https://doi.org/10.1021/jasms.3c00033
J. Am. Soc. Mass Spectrom. 2023, 34, 1305−1314

relative cellular composition of each glomerulus. For example, the relative cellular composition of each glomerulus can be dependent on the depth of the plane at which the glomeruli were sectioned as well as their disease severity. The distinct morphological characteristics of glomeruli from each cluster shown with the PAS stain are indicative of cellular heterogeneity, which is expected to produce unique molecular profiles. Diseased glomeruli can also be observed in the autofluorescence image. This is likely due to extracellular matrix accumulation (e.g., collagen and fibronectin) in sclerosed glomeruli, causing them to be more autofluorescent and stain darker with PAS (Figure S12).[46,47]

Examining the average spectra reveals broad changes in the relative intensity of the detected lipids (Figure S13) in glomeruli that were found to be healthy compared to diseased. This is also reflected in the individual ion images, which show different spatial patterns for healthy and diseased glomeruli, as shown in Figure 4B and Figure S14. For example, the distributions of sphingomyelin (SM) (18:1;2O/16:0) with a loss of a methyl group (m/z 687.5441) and phosphatidylserine (PS) (18:0_18:1) (m/z 788.5444) are altered in the diseased glomerulus when compared to healthy. The ion images show that there is a higher intensity of SM (18:1;2O/16:0) in the diseased glomerulus than the healthy glomerulus. These lipids were identified with LC-MS/MS and mass accuracy as described in Methods S1. Details of molecular identifications can be found in Table S4 for selected ions. This table includes MALDI m/z, LC-MS/MS m/z, theoretical m/z, ppm error for both LC-MS/MS and MALDI, average retention time, lipid name, and adduct type. A LC-MS/MS spectrum and a MALDI on tissue MS/MS spectrum of SM (18:1;2O/16:0) is shown in Figure S1, and the LC-MS/MS spectrum of PS (18:0_18:1) as well as the other ions are shown in Figures S2−S10.

To visualize molecular subregions within the glomeruli, we used k-means clustering and segmentation at the IMS pixel level (Figure 4). This multivariate analysis was performed on all pixels within the imaged glomeruli (Figure S15). Comparisons to complementary microscopy and individual ion images can be found in Figures 4A and S14, respectively. Clustering in this manner finds pixels with distinct molecular profiles within all glomeruli and, when visualized, can help find spatial patterns and ratios of each cluster between healthy and diseased glomeruli (Figure 4C,D). For example, SM (18:1;2O/16:0), PS (18:0_18:1), and phosphatidic acid (PA) (36:1) (m/z 701.5108) are more prominent in the pink cluster (k = 2) as compared to the orange cluster (k = 1). Molecular profiles for each cluster can be found in Figure S16. This workflow showcases the ability of high spatial resolution MALDI IMS to uncover localized lipidomic differences within individual FTUs, in this case, the ability to detect subregions within each glomerulus.

An additional 10 ion images of four glomeruli with their respective k-means clustering and UMAP are shown in Figure S14. Furthermore, a molecular profile from each pixel-wise k-means cluster (k = 6) is shown in Figure S16 with an enhanced region between m/z 650 and 900, and Figure S11 shows the molecular profiles from m/z 650 to 900 for each UMAP k-means cluster.

The observed molecular differences in the analyzed glomeruli may be related to the severity of glomerulosclerosis. Glomerulosclerosis can occur in healthy, aging patients as well as patients with an underlying disease.[48−52] The affected glomeruli typically perform hyperfiltration and can leak excess protein into urine.[46,47,53] Our microscopy-driven approach for high spatial resolution MALDI IMS could provide a way to rapidly screen disease severity in large numbers of glomeruli across sizable sample cohorts.

CONCLUSIONS

This work demonstrates microscopy-driven high spatial resolution MALDI IMS of segmented glomeruli in a whole slide human kidney tissue section. Our optimized method was found to enable 5 μm MALDI IMS with minimal oversampling. Autofluorescence microscopy was used to automatically segment glomeruli and to determine IMS measurement regions, improving data acquisition time almost 10× compared to imaging the entire tissue at 5 μm pixel size. Unsupervised machine learning methods were used to explore the lipidomic trends underlying the measurements, and some were found to differentiate healthy and diseased glomeruli. These observations were subsequently confirmed by using complementary stained microscopy. Further analysis was done to visualize molecular heterogeneity and distinguish subregions within the individual glomeruli. Specifically, the ability to perform both high spatial resolution and high-throughput MALDI imaging concurrently using this approach allowed molecular patterns associated with glomerulosclerosis across large human kidney tissue sections to be captured.

Although this technical demonstration of our automated workflow is necessary for comprehensive molecular imaging of glomeruli, similar approaches are even more critical for other kidney FTUs that are present at higher numbers, such as proximal tubules in the kidney or colonic crypts. Strategies for automated, high throughput IMS analysis are also critical for studies that require analysis of large cohorts of samples. Specifically for this case study on the human kidney, further development is necessary to link observed patterns to specific cell types within the glomerulus, and this will likely require integration with immunofluorescence and more advanced data mining (e.g., using Tideman et al.'s approach[54]). The workflow presented herein is a key advancement in making these studies practical. Multimodal molecular imaging technologies that provide both high spatial resolution analysis and deep molecular coverage while also delivering results rapidly will be critical for next-generation biomedical research applications. Microscopy-driven high spatial resolution MALDI IMS offers the potential to more thoroughly characterize diseases of the kidney, or any organ system, providing a systems biology view of FTUs, cellular neighborhoods, and cell types *in situ*.

ASSOCIATED CONTENT

Supporting Information

The Supporting Information is available free of charge at https://pubs.acs.org/doi/10.1021/jasms.3c00033.

The pathology assessment of the human kidney sample, additional instrument parameters, LC-MS/MS and on-tissue MALDI MS/MS workflow, MS/MS spectra of the 10 most abundant peaks, table of lipid identifications, averages and standard deviations from 5 μm versus 10 μm experiment, molecular profiles for each k-means cluster based on UMAP embedding, PAS and autofluorescence images of diseased and healthy glomeruli with accompanying annotated glomeruli, enhanced spectra of healthy and diseased glomeruli, additional ion images, k-means of each glomerulus and

https://doi.org/10.1021/jasms.3c00033
J. Am. Soc. Mass Spectrom. 2023, 34, 1305−1314

their *in situ* position on the tissue section, and molecular profiles for each pixel-wise *k*-means cluster (ZIP)

AUTHOR INFORMATION

Corresponding Author

Jeffrey M. Spraggins − *Mass Spectrometry Research Center, Department of Chemistry, Department of Biochemistry, and Department of Cell and Developmental Biology, Vanderbilt University, Nashville, Tennessee 37232, United States;* orcid.org/0000-0001-9198-5498; Email: jeff.spraggins@vanderbilt.edu

Authors

Allison B. Esselman − *Mass Spectrometry Research Center and Department of Chemistry, Vanderbilt University, Nashville, Tennessee 37232, United States;* orcid.org/0000-0002-4122-6773

Nathan Heath Patterson − *Mass Spectrometry Research Center and Department of Biochemistry, Vanderbilt University, Nashville, Tennessee 37232, United States;* orcid.org/0000-0002-0064-1583

Lukasz G. Migas − *Mass Spectrometry Research Center, Vanderbilt University, Nashville, Tennessee 37232, United States; Delft Center for Systems and Control, Delft University of Technology, 2628 Delft, The Netherlands;* orcid.org/0000-0002-1884-6405

Martin Dufresne − *Mass Spectrometry Research Center and Department of Biochemistry, Vanderbilt University, Nashville, Tennessee 37232, United States;* orcid.org/0000-0002-1731-3666

Katerina V. Djambazova − *Mass Spectrometry Research Center and Department of Cell and Developmental Biology, Vanderbilt University, Nashville, Tennessee 37232, United States;* orcid.org/0000-0002-2680-9014

Madeline E. Colley − *Mass Spectrometry Research Center and Department of Biochemistry, Vanderbilt University, Nashville, Tennessee 37232, United States;* orcid.org/0000-0002-9515-3493

Raf Van de Plas − *Mass Spectrometry Research Center and Department of Biochemistry, Vanderbilt University, Nashville, Tennessee 37232, United States; Delft Center for Systems and Control, Delft University of Technology, 2628 Delft, The Netherlands;* orcid.org/0000-0002-2232-7130

Complete contact information is available at: https://pubs.acs.org/10.1021/jasms.3c00033

Notes

The authors declare no competing financial interest.

ACKNOWLEDGMENTS

Research reported in this publication was supported by the National Institutes of Health (NIH)'s Common Fund, National Institute of Diabetes and Digestive and Kidney Diseases (NIDDK), and the Office of the Director (OD) under Award Numbers U54DK134302 and U01DK133766 (J.M.S. and R.V.), by NIH's Common Fund, National Eye Institute, and the Office of the Director (OD) under Award Number U54EY032442 (J.M.S. and R.V.), NIH's National Institute on Aging (NIA) under Award Number R01AG078803 (J.M.S. and R.V.), and by the National Science Foundation Major Research Instrument Program CBET − 1828299 (J.M.S.). The research was furthermore made possible in part by grant numbers 2021-240339 and 2022-309518 (L.G.M. and R.V.) from the Chan Zuckerberg Initiative DAF, an advised fund of Silicon Valley Community Foundation, and supported by the Nederlandse Organisatie voor Wetenschappelijk Onderzoek (NWO), ZonMw, FLAG-ERA, and the European Commission through FLAG-ERA III JTC project SMART BRAIN (NWO 680-91-319) under Specific Grant Agreement No. 785907 (Human Brain Project SGA2) (R.V.). The content is solely the responsibility of the authors and does not necessarily represent the official views of the funders. The authors would like to thank Jamie Allen for processing and preparing frozen tissue blocks of human kidney tissue as well as Dr. Haichun Yang and Dr. Agnes Fogo for the pathological assessment of the sample. The table of contents figure and Figure S11 were created using images from BioRender.com (Agreement number: IX24WQOGMA).

REFERENCES

(1) Song, R.; Yosypiv, I. v. Development of the Kidney Medulla. *Organogenesis* **2012**, *8* (1), 10−17.

(2) Tryggvason, K.; Wartiovaara, J. How Does the Kidney Filter Plasma? *Physiology* **2005**, *20*, 96−101.

(3) Samuel, T.; Hoy, W. E.; Douglas-Denton, R.; Hughson, M. D.; Bertram, J. F. Applicability of the Glomerular Size Distribution Coefficient in Assessing Human Glomerular Volume: The Weibel and Gomez Method Revisited. *J. Anat.* **2007**, *210*, 578−582.

(4) Gessel, M. M.; Spraggins, J. M.; Voziyan, P. A.; Abrahamson, D. R.; Caprioli, R. M.; Hudson, B. G. Two Specific Sulfatide Species Are Dysregulated during Renal Development in a Mouse Model of Alport Syndrome. *Lipids* **2019**, *54*, 411−418.

(5) Grove, K. J.; Voziyan, P. A.; Spraggins, J. M.; Wang, S.; Paueksakon, P.; Harris, R. C.; Hudson, B. G.; Caprioli, R. M. Diabetic Nephropathy Induces Alterations in the Glomerular and Tubule Lipid Profiles. *J. Lipid Res.* **2014**, *55* (7), 1375−1385.

(6) Eddy, S.; Mariani, L. H.; Kretzler, M. Integrated Multi-Omics Approaches to Improve Classification of Chronic Kidney Disease. *Nat. Rev. Nephrol* **2020**, *16*, 657−668.

(7) Caprioli, R. M.; Farmer, T. B.; Gile, J. Molecular Imaging of Biological Samples: Localization of Peptides and Proteins Using MALDI-TOF MS. *Anal. Chem.* **1997**, *69* (23), 4751−4760.

(8) Stewart, B. J.; Clatworthy, M. R. Applying Single-Cell Technologies to Clinical Pathology: Progress in Nephropathology. *J. Pathol.* **2020**, *250*, 693−704.

(9) Lin, H.-T.; Cheng, M.-L.; Lo, C.-J.; Lin, G.; Liu, F.-C. Metabolomic Signature of Diabetic Kidney Disease in Cerebrospinal Fluid and Plasma of Patients with Type 2 Diabetes Using Liquid Chromatography-Mass Spectrometry. *Diagnostics* **2022**, *12* (11), 2626.

(10) Aoki, M.; Kang, D.; Katayama, A.; Kuwahara, N.; Nagasaka, S.; Endo, Y.; Terasaki, M.; Kunugi, S.; Terasaki, Y.; Shimizu, A. Optimal Conditions and the Advantages of Using Laser Microdissection and Liquid Chromatography Tandem Mass Spectrometry for Diagnosing Renal Amyloidosis. *Clin. Exp. Nephrol.* **2018**, *22*, 871−880.

(11) Prentice, B. M.; Caprioli, R. M.; Vuiblet, V. Label-Free Molecular Imaging of the Kidney. *Kidney Int.* **2017**, *92* (3), 580−598.

(12) Zemaitis, K. J.; Velickovic, D.; Kew, W.; Fort, K. L.; Reinhardt-Szyba, M.; Pamreddy, A.; Ding, Y.; Kaushik, D.; Sharma, K.; Makarov, A. A.; Zhou, M.; Paša-Tolić, L. Enhanced Spatial Mapping of Histone Proteoforms in Human Kidney Through MALDI-MSI by High-Field UHMR-Orbitrap Detection. *Anal. Chem.* **2022**, *94*, 12604−12613.

(13) Walter, A.; Paul-Gilloteaux, P.; Plochberger, B.; Sefc, L.; Verkade, P.; Mannheim, J. G.; Slezak, P.; Unterhuber, A.; Marchetti-Deschmann, M.; Ogris, M.; Bühler, K.; Fixler, D.; Geyer, S. H.; Weninger, W. J.; Glösmann, M.; Handschuh, S.; Wanek, T. Correlated Multimodal Imaging in Life Sciences: Expanding the Biomedical Horizon. *Front. Phys.* **2020**, *8*, 1−28.

(14) Buchberger, A. R.; DeLaney, K.; Johnson, J.; Li, L. Mass Spectrometry Imaging: A Review of Emerging Advancements and Future Insights. *Anal. Chem.* **2018**, *90*, 240−265.
(15) Lukowski, J. K.; Pamreddy, A.; Velickovic, D.; Zhang, G.; Pasa-Tolic, L.; Alexandrov, T.; Sharma, K.; Anderton, C. R. Storage Conditions of Human Kidney Tissue Sections Affect Spatial Lipidomics Analysis Reproducibility. *J. Am. Soc. Mass Spectrom.* **2020**, *31*, 2538−2546.
(16) Mcmillen, J. C.; Gutierrez, D. B.; Judd, A. M.; Spraggins, J. M.; Caprioli, R. M. Enhancement of Tryptic Peptide Signals from Tissue Sections Using MALDI IMS Postionization (MALDI-2). *J. Am. Soc. Mass Spectrom.* **2021**, *32*, 2583−2591.
(17) Neumann, E. K.; Migas, L. G.; Allen, J. L.; Caprioli, R. M.; van de Plas, R.; Spraggins, J. M. Spatial Metabolomics of the Human Kidney Using MALDI Trapped Ion Mobility Imaging Mass Spectrometry. *Anal. Chem.* **2020**, *92*, 13084−13091.
(18) Spraggins, J. M.; Djambazova, K. v; Rivera, E. S.; Migas, L. G.; Neumann, E. K.; Fuetterer, A.; Suetering, J.; Goedecke, N.; Ly, A.; van de Plas, R.; Caprioli, R. M. High-Performance Molecular Imaging with MALDI Trapped Ion-Mobility Time-of-Flight (TimsTOF) Mass Spectrometry. *Anal. Chem.* **2019**, *91*, 14552.
(19) Martín-Saiz, L.; Mosteiro, L.; Solano-Iturri, J. D.; Rueda, Y.; Martín-Allende, J.; Imaz, I.; Olano, I.; Ochoa, B.; Fresnedo, O.; Fernández, J. A.; Larrinaga, G. High-Resolution Human Kidney Molecular Histology by Imaging Mass Spectrometry of Lipids. *Anal. Chem.* **2021**, *93*, 9364−9372.
(20) Taylor, M. J.; Lukowski, J. K.; Anderton, C. R. Spatially Resolved Mass Spectrometry at the Single Cell: Recent Innovations in Proteomics and Metabolomics. *J. Am. Soc. Mass Spectrom.* **2021**, *32*, 872−894.
(21) Dueñas, M. E.; Essner, J. J.; Lee, Y. J. 3D MALDI Mass Spectrometry Imaging of a Single Cell: Spatial Mapping of Lipids in the Embryonic Development of Zebrafish. *OPEN. Sci. Rep* **2017**, *7* (14946), 1−10.
(22) Holzlechner, M.; Strasser, K.; Zareva, E.; Steinhauser, L.; Birnleitner, H.; Beer, A.; Bergmann, M.; Oehler, R.; Marchetti-Deschmann, M. In Situ Characterization of Tissue-Resident Immune Cells by MALDI Mass Spectrometry Imaging. *J. Proteome Res.* **2017**, *16*, 65−76.
(23) Puolitaival, S. M.; Burnum, K. E.; Cornett, D. S.; Caprioli, R. M. Solvent-Free Matrix Dry-Coating for MALDI Imaging of Phospholipids. *J. Am. Soc. Mass Spectrom.* **2008**, *19*, 882−886.
(24) Anderson, D. M. G.; Floyd, K. A.; Barnes, S.; Clark, J. M.; Clark, J. I.; Mchaourab, H.; Schey, K. L. A Method to Prevent Protein Delocalization in Imaging Mass Spectrometry of Non-Adherent Tissues: Application to Small Vertebrate Lens Imaging. *Anal Bioanal Chem.* **2015**, *407*, 2311−2320.
(25) Spivey, E. C.; McMillen, J. C.; Ryan, D. J.; Spraggins, J. M.; Caprioli, R. M. Combining MALDI-2 and Transmission Geometry Laser Optics to Achieve High Sensitivity for Ultra-High Spatial Resolution Surface Analysis. *J.Mass Spectrom.* **2019**, *54* (4), 366−370.
(26) Niehaus, M.; Soltwisch, J.; Belov, M. E.; Dreisewerd, K. Transmission-Mode MALDI-2 Mass Spectrometry Imaging of Cells and Tissues at Subcellular Resolution. *Nat. Methods* **2019**, *16*, 925−931.
(27) Bien, T.; Bessler, S.; Dreisewerd, K.; Soltwisch, J. Transmission-Mode MALDI Mass Spectrometry Imaging of Single Cells: Optimizing Sample Preparation Protocols. *Anal. Chem.* **2021**, *93*, 4513−4520.
(28) Zhu, X.; Xu, T.; Peng, C.; Wu, S. Advances in MALDI Mass Spectrometry Imaging Single Cell and Tissues. *Front Chem.* **2022**, *9*, 1−27.
(29) Patterson, N. H.; Tuck, M.; Lewis, A.; Kaushansky, A.; Norris, J. L.; van de Plas, R.; Caprioli, R. M. Next Generation Histology-Directed Imaging Mass Spectrometry Driven by Autofluorescence Microscopy. *Anal. Chem.* **2018**, *90*, 12404−12413.
(30) Patterson, N. H.; Neumann, E. K.; Sharman, K.; Allen, J.; Harris, R.; Fogo, A. B.; de Caestecker, M.; Caprioli, R. M.; Van de Plas, R.; Spraggins, J. M. Autofluorescence Microscopy as a Label-Free Tool for Renal Histology and Glomerular Segmentation. *bioRxiv*, July 18, 2021. DOI: 10.1101/2021.07.16.452703.
(31) Neumann, E. K.; Patterson, N. H.; Allen, J. L.; Migas, L. G.; Yang, H.; Brewer, M.; Anderson, D. M.; Harvey, J.; Gutierrez, D. B.; Harris, R. C.; deCaestecker, M. P.; Fogo, A. B.; van de Plas, R.; Caprioli, R. M.; Spraggins, J. M. Protocol for Multimodal Analysis of Human Kidney Tissue by Imaging Mass Spectrometry and CODEX Multiplexed Immunofluorescence. *STAR Protoc* **2021**, *2*, 100747.
(32) Anderson, D.; Dufresne, M.; Messinger, J. D.; Allen, J.; Djambazova, K. V.; Kruse, A.; Curcio, C. A.; Schey, K. L.; Caprioli, R. M.; Spraggins, J. Matrix Sublimation via In-House Developed Sublimation Apparatus. *protocols.io*. https://www.protocols.io/view/matrix-sublimation-via-in-house-developed-sublimat-n92ldpyn9l5b/v1(accessed on April 5, 2023).
(33) Neumann, E.; Allen, J.; Patterson, H.; Gutierrex, D.; Spraggins, J. Post-IMS Autofluorescence Microscopy. *protocols.io*. https://www.protocols.io/view/post-ims-autofluorescence-microscopy-3byl47kx2lo5/v1(accessed on January 12, 2023).
(34) Neumann, E.; Allen, J.; Kruse, A. R. S.; Harvey, J.; Brewer, M.; Romer, C.; Caestecker, M. de.; Spraggins, J. PAS Staining of Fresh Frozen or Paraffin Embedded Human Kidney Tissue V.3. *protocols.io*. DOI: 10.17504/protocols.io.buaknscw.
(35) Bankhead, P.; Loughrey, M. B.; Fernández, J. A.; Dombrowski, Y.; Mcart, D. G.; Dunne, P. D.; Mcquaid, S.; Gray, R. T.; Murray, L. J.; Coleman, H. G.; James, J. A.; Salto-Tellez, M.; Hamilton, P. W. QuPath: Open Source Software for Digital Pathology Image Analysis. *Sci. Rep* **2017**, *7* (16878), 1−7.
(36) Patterson, H.; Manz, T. *NHPatterson/wsireg: wsireg v0.3.0*. Zenodo. DOI: 10.5281/zenodo.5518238.
(37) Sud, M.; Fahy, E.; Cotter, D.; Brown, A.; Dennis, E.; Glass, C.; Murphy, R.; Raetz, C.; Russell, D.; Suramaniam, S. *Lipid Maps*. Nucleic Acid Research. https://www.lipidmaps.org/how-to-cite(accessed on January 17, 2023).
(38) Patterson, H. *NHPatterson/napari-imsmicrolink: IMS MicroLink v0.1.7*. Zenodo. DOI: 10.5281/zenodo.6562052.
(39) Patterson, N. H.; Tuck, M.; van de Plas, R.; Caprioli, R. M. Advanced Registration and Analysis of MALDI Imaging Mass Spectrometry Measurements through Autofluorescence Microscopy. *Anal. Chem.* **2018**, *90* (21), 12395−12403.
(40) *Bruker SDK (v2.21)*. https://www.bruker.com/protected/de/services/software-downloads/mass-spectrometry/raw-data-access-libraries.html(accessed on January 9, 2023).
(41) Monchamp, P.; Andrade-Cetto, L.; Zhang, J. Y.; Henson, R. *Signal Processing Methods for Mass Spectrometry*; Alterovitz, G., Ramoni, M. F., Eds.; Artech House Publishers, 2007.
(42) Verbeeck, N.; Caprioli, R. M.; van de Plas, R. Unsupervised Machine Learning For Exploratory Data Analysis In Imaging Mass Spectrometry. *Mass Spectrom Rev.* **2020**, *39* (3), 245−291.
(43) McInnes, L.; Healy, J.; Melville, J. UMAP: Uniform Manifold Approximation and Projection for Dimension Reduction. *arXiv*, February 9, 2018. DOI: 10.48550/arxiv.1802.03426.
(44) Pedregosa, F.; Varoquaux, G.; Gramfort, A.; Michel, V.; Thirion, B.; Grisel, O.; Blondel, M.; Prettenhofer, P.; Weiss, R.; Dubourg, V.; Vanderplas, J.; Passos, A.; Cournapeau, D.; Brucher, M.; Perrot, M.; Duchesnay, E. Scikit-Learn: Machine Learning in Python. *J. Mach. Learn. Res.* **2011**, *12*, 2825−2830.
(45) Bowman, A. P.; Bogie, J. F. J.; Hendriks, J. J. A.; Haidar, M.; Belov, M.; Heeren, R. M. A.; Ellis, S. R. Evaluation of Lipid Coverage and High Spatial Resolution MALDI-Imaging Capabilities of Oversampling Combined with Laser Post-Ionisation. *Anal Bioanal Chem.* **2020**, *412*, 2277−2289.
(46) Nagata, M.; Kobayashi, N.; Hara, S. Focal Segmental Glomerulosclerosis; Why Does It Occur Segmentally? *Eur. J. Physiol* **2017**, *469*, 983−988.
(47) Freedman, B. I.; Cohen, A. H. Hypertension-Attributed Nephropathy: What's in a Name. *Nephrology* **2016**, *12*, 27−36.
(48) Kremers, W. K.; Denic, A.; Lieske, J. C.; Alexander, M. P.; Kaushik, V.; Elsherbiny, H. E.; Chakkera, H. A.; Poggio, E. D.; Rule, A. D. Distinguishing Age-Related from Disease-Related Glomerulo-

sclerosis on Kidney Biopsy: The Aging Kidney Anatomy Study. *Nephrol. Dial. Transplant.* **2015**, *30* (12), 2034−2039.
(49) Kaplan, C.; Pasternack, B.; Shah, H.; Gallo, G. Age-Related Incidence of Sclerotic Glomeruli in Human Kidneys. *Am. J. Pathol.* **1975**, *80* (2), 227−234.
(50) Hommos, M. S.; Glassock, R. J.; Rule, A. D. Structural and Functional Changes in Human Kidneys with Healthy Aging. *J. Am. Soc. of Nephrol.* **2017**, *28* (10), 2838−2844.
(51) Anderson, S.; Brenner, B. M. Effects of Aging on the Renal Glomerulus. *Am. J. Med.* **1986**, *80* (3), 435−442.
(52) Rule, A. D.; Amer, H.; Cornell, L. D.; Taler, S. J.; Cosio, F. G.; Kremers, W. K.; Textor, S. C.; Stegall, M. D. The Association between Age and Nephrosclerosis on Renal Biopsy among Healthy Adults. *Ann. Int. Med.* **2010**, *152* (9), 561−567.
(53) Hommos, M. S.; Zeng, C.; Liu, Z.; Troost, J. P.; Rosenberg, A. Z.; Palmer, M.; Kremers, W. K.; Cornell, L. D.; Fervenza, F. C.; Barisoni, L.; Rule, A. D. Global Glomerulosclerosis with Nephrotic Syndrome; the Clinical Importance of Age Adjustment. *Kidney Int.* **2018**, *93* (5), 1175−1182.
(54) Tideman, L. E.; Migas, L. G.; Djambazova, K. V.; Patterson, N. H.; Caprioli, R. M.; Spraggins, J. M.; Van de Plas, R. Automated Biomarker Candidate Discovery in Imaging Mass Spectrometry Data through Spatially Localized Shapley Additive Explanations. *Analytica Chemica Acta* **2021**, *1177*, 338522.

https://doi.org/10.1021/jasms.3c00033
J. Am. Soc. Mass Spectrom. 2023, 34, 1305−1314